Hindawi
Advances in Mathematical Physics
Volume 2023, Article ID 8426825, 15 pages
https://doi.org/10.1155/2023/8426825

Research Article

Use of Finite Element Method for Free Convection of Nanofluids between a Rectangular Enclosure and a Sinusoidal Cylinder Using Buongiorno's Two-Phase Model

Abeer Alhashash[1] **and Habibis Saleh**[2]

[1]*Department of Mathematics, College of Science, Jouf University, P.O. Box 2014, Sakaka 24241, Saudi Arabia*
[2]*Mathematics Education Department, Universitas Islam Negeri Sultan Syarif Kasim Riau, Pekanbaru, Indonesia*

Correspondence should be addressed to Abeer Alhashash; ahashash@ju.edu.sa

Received 12 October 2022; Revised 2 December 2022; Accepted 6 April 2023; Published 17 April 2023

Academic Editor: Shuo Yin

In this study, the free convection of nanofluids between a rectangular enclosure and a sinusoidal cylinder is numerically analyzed using the finite element method (FEM). Two-phase Buongiorno's formulation was used to model the fluid layer, and Brinkman-Forchheimer equation was used to formulate the porous layer. The enclosure has a low temperature, while the cylinder is maintained at a high temperature. The governing equations are expressed in PDEs and converted into weak formulations (Galerkin FEM). In numerical simulations, the average concentration, the amplitude of undulated cylinder, the number of undulated, and the Rayleigh number are investigated. It is observed that the homogeneous nanofluid model could be valid for low heating intensity with higher waviness frequency and/or higher amplitude. The higher the alumina concentration, the higher the heat transfer rate. The heat transfer rate can be boosted by up to 13% by suspending 1% alumina particles. The heat transfer enhancement decreases with increasing the amplitude and/or increasing the waviness number.

1. Introduction

The phenomena of natural convection induced by a high cylinder temperature inside a low enclosure temperature are analyzed. One of the applications happens in a pipe carrying hot fluid that passes through an enclosed space. The enclosure has saturated porous adiabatic material to decrease the thermal gradient from the cylinder. The flow movement between a pipe and the environment of fluid space induces a pattern of convection cells. In each cell, the fluid circulates in a path and the direction of circulation is contrary with successive vortices. Oosthuizen and Naylor [1] studied the bottom and sides of the enclosure in insulated condition, and the above wall is cold while the cylinder is constantly heated. They found that small change in the Nusselt number with changing the cylinder radius. Misirlioglu [2] investigated the active cylinder put in the middle enclosure and conclude that the rotating cylinder enhances the heat transfer in the square enclosure. Saleh and Hashim [3] filled the enclosure with nanofluids. They concluded that there is an optimum radius, below which adding its size, increases the fluid movements and above which the cylinder size reduces the fluid movement. Alhashash [4] concluded that the heat transfer enhancement for the half heating and high value of permeability is at the denser nanoparticle volume fraction. Tayebi and Chamkha [5] and Tayebi et al. [6] reported that the convective flow circulation of nanofluid in a horizontal elliptical porous annulus is improved as the Darcy number and porosity increase.

Undulated surfaces are utilized in many thermal systems as a means of enhancing the mass and heat transfers, such as solar collectors, microelectronic devices, electric machinery, water storage, and condensers in refrigerators. The published works on the wavy walls have shown that this problem is limited due to the complexness of the mesh generation and parametric analyses of the impacts of several major variables. Murthy et al. [7] investigated the impact of the waviness at the horizontal wall and found that the convection intensity

is decreased by using the wavy wall. Kumar [8] showed that the high undulation frequency of the vertical wall enhances the natural convection. Later, Kumar [9] reported that the heating produces a complex oscillatory structure of period equivalent to the wavy wall. Misirlioglu et al. [10] utilized the sinusoidal undulation and compared their findings with those reported in the previous result for a square enclosure with flat walls. They investigated some values of heating intensity, aspect ratio, and waviness factors. Later, Misirlioglu et al. [11] found that the convective flow was found to be sensitive on undulation for inclination less than 45° at high heating intensity. The waviness modified the thermal distributions illustrated by Khanafer et al. [12]. Mushatet [13] considered double undulation of the side walls having differentially heated and concluded that the orientation angle, the number, and the amplitude of corrugation and Rayleigh number have a considerably impact on the convective flow. Mansour et al. [14] looked at the effect of radiation when conditions are not in equilibrium and concluded that the heat transfer decreases by increasing the thermal conductivity ratio. Sompong and Witayangkurn [15] found that convective flows were slightly affected by varying the corrugation number. Sheremet et al. [16] reported the heat transfer improvement by dispersing nanoparticle, heating intensity, undulated number, and thermal deviation quantity. Cheong et al. [17] analyzed the impact of trigonometrical external heating and inner heat combustion to the wavy wall. Hoghoughi et al. [18] studied the effect of corrugation parameters on the free convection of nanoliquid over a circular heater under nonequilibrium state. They concluded that when the circular heater is raised, the heat transfer is less at smaller undulation amplitudes. Alhashash and Saleh [19] considered the effect of undulated surfaces and nanoparticle parameters. Alhashash [20] found that the thermal performance of the corrugated surface is slightly enhanced under specific conditions. Alsabery et al. [21] reported that increasing the length of the heater might enhance heat transfer within the wavy enclosure with the rotating cylinder.

Prior research almost exclusively concentrated on convection in porous enclosures with smooth walls, as opposed to flow and heat transfer in walls with undulations. This work analyzes the effect of undulations on the flow and convective heat transfer properties of water alumina in an enclosure with a sinusoidal hot cylinder. The investigated geometry can be utilized to passively regulate heat transmission in an evacuated-tube solar absorber. Accordingly, the main novelty of this study is the investigation of the coeffect of waviness and nanoparticles on fluid circulation within a porous cavity. In addition, the simultaneous influence of the cylinder surface and the Brinkman-Forchheimer on heat transfer characteristics is studied using the two-phase mixture model. The two-phase nanofluid model was previously adopted by Alsabery et al. [22], Alsabery et al. [23], Ghasemian et al. [24], and Hoseininejad et al. [25]. Arrangements of corrugated cylinder were considered by Nabavizadeh et al. [26], Sheikholeslami et al. [27], Hatami and Safari [28], Hashim et al. [29], Jabbaripour et al. [30], and Tayebi and Chamkha [31] for nonporous case and found the streamlines and isotherm pattern sensitive on the waviness surface.

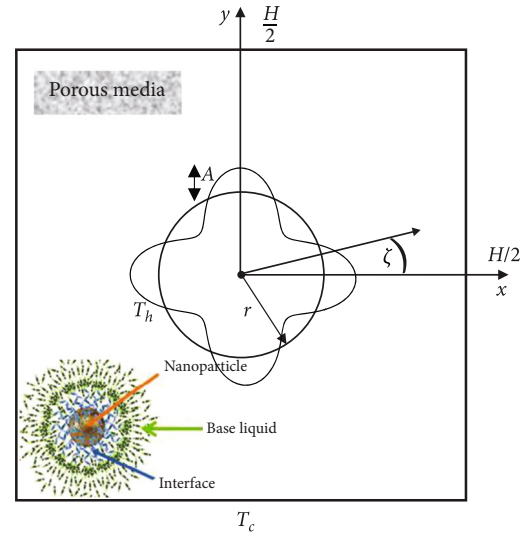

Figure 1: Diagrammatic illustration of the model.

2. Mathematical Formulation

A 2D schematic model of an enclosure having a sinusoidal hot cylinder is presented in Figure 1. The fluids within the annulus are water-based nanofluids having alumina nanoparticles. The outer walls were maintained at a low temperature. When the alumina is suspended in the water, Brownian motion happens from the relative velocity at the interface as illustrated in the schematic representation. When there are no turbulence effects, it follows Buongiorno's model. Buongiorno evaluated the impacts of various slip mechanisms between the base fluid and nanoparticles that are gravity, thermophoresis, Brownian diffusion, inertia, the Magnus impact, fluid drainage, and diffusiophoresis. The most influential mechanisms on nanofluid flow and heat transmission, which can affect nanoparticle concentration fluctuations, were proven to be thermophoresis and Brownian diffusion. The cylinder having radius r is put in the middle of the enclosure. The sine wavy profile of the cylinder surface follows the relation:

$$r(\eta) = r_b + A \sin(N\zeta), \tag{1}$$

where r_{in} is the base radius, parameters A and N are amplitude and number of corrugations, respectively, and ζ is the rotation coordinate. The thermophysical properties of the applied materials are tabulated in Table 1 [32].

Under the effect of the buoyancy force, the cylinder surface and enclosure at different levels of temperature bring a free convection problem. The Brinkman-Forchheimer model is assumed valid for the porous layer, and the Boussinesq approximation is applied for density variation due to differentially heated. A nanofluid with Newtonian properties fills the pores of the porous material. Using a thermal equilibrium model and accounting for Brownian nanoparticle kinematics and thermophoresis factors, energy equations for the fluid phase of a porous media are derived. Based on

Table 1: The materials used and their thermophysical properties [32].

Materials	ρ (kg/m^3)	μ (N s/m^2)	k (W m^{-1} K^{-1})	C_p (J/kg K)	β (1/K)	d (m)
Water	993	0.00069	0.628	4.178	0.00036	3.85e-10
Alumina	3970	—	40	765	0.00085	2.5e-9

these considerations, the continuity, the momentum, and the energy equations are stated as follows [33, 34]:

$$\frac{\partial u}{\partial x} + \frac{\partial v}{\partial y} = 0, \tag{2}$$

$$\rho_{nf}\frac{u}{\varepsilon^2}\frac{\partial u}{\partial x} + \frac{v}{\varepsilon^2}\frac{\partial u}{\partial y} = -\frac{\partial p}{\partial x} + \frac{\mu_{nf}}{\varepsilon}\left(\frac{\partial^2 u}{\partial x^2} + \frac{\partial^2 u}{\partial y^2}\right) - \frac{150\mu_{nf}(1-\varepsilon)^2}{d^2\varepsilon^3}u - \frac{262.5d(1-\varepsilon)^2}{d^2}\frac{\sqrt{u^2+v^2}}{\varepsilon^3}, \tag{3}$$

$$\rho_{nf}\frac{u}{\varepsilon^2}\frac{\partial v}{\partial x} + \frac{v}{\varepsilon^2}\frac{\partial v}{\partial y} = -\frac{\partial p}{\partial y} + \frac{\mu_{nf}}{\varepsilon}\left(\frac{\partial^2 v}{\partial x^2} + \frac{\partial^2 v}{\partial y^2}\right) - \frac{150\mu_{nf}(1-\varepsilon)^2}{d^2\varepsilon^3}v - \frac{262.5d(1-\varepsilon)^2}{d^2}\frac{\sqrt{u^2+v^2}}{\varepsilon^3} + (\rho\beta)_{nf}g\frac{\partial T_{nf}}{\partial x}, \tag{4}$$

$$\frac{(\rho C_p)_{nf}}{\varepsilon}\left[u\frac{\partial T_{nf}}{\partial x} + v\frac{\partial T_{nf}}{\partial y}\right] = -k_{nf}\left(\frac{\partial^2 T_{nf}}{\partial x^2} + \frac{\partial^2 T_{nf}}{\partial y^2}\right) - C_{p,p}J_{np}\cdot\nabla T_{nf}, \tag{5}$$

$$u\frac{\partial C_{nf}}{\partial x} + v\frac{\partial C_{nf}}{\partial y} = -\frac{\varepsilon}{\rho_{np}}\nabla\cdot J_{np}, \tag{6}$$

where velocities are zero on the enclosure and cylinder surface. The thermal boundary conditions are

$$\begin{aligned} &T_{nf} = T_c \text{ on left, right, top, and bottom walls,}\\ &T_{nf} = T_h \text{ on cylinder surface,} \end{aligned} \tag{7}$$

where symbol g is the gravity acceleration, C_{nf} is the concentration of nanoparticles, and J_{np} is the solid nanoparticle mass flux. Based on two phase, Buongiorno's model nanoparticle mass flux can be stated as follows:

$$J_{np} = J_{p,B} + J_{p,T}, \tag{8}$$

$$J_{p,B} = -\rho_{np}D_B\nabla C_{nf}, D_B = \frac{k_b T_{nf}}{3\pi\mu_{bf}d_{np}}, \tag{9}$$

$$J_{p,T} = -\rho_{np}D_T\nabla T_{nf}, D_T = 0.26\frac{k_{bf}}{2k_{bf}+k_{np}}\frac{\mu_{bf}}{\rho_{bf}T_{nf}}C_{nf}. \tag{10}$$

The nanofluid heat capacitance $(\rho C_p)_{nf}$ is given as

$$(\rho C_p)_{nf} = (1-\phi)(\rho C_p)_{bf} + \phi(\rho C_p)_{np}. \tag{11}$$

The thermal diffusivity of the nanofluids α_{nf} is evaluated as

$$\alpha_{nf} = \frac{k_{nf}}{(\rho C_p)_{nf}}. \tag{12}$$

The density of the nanofluids ρ_{nf} can be evaluated:

$$\rho_{nf} = (1-\phi)\rho_{bf} + \phi\rho_{np}. \tag{13}$$

The nanofluid thermal coefficient is modelled as

$$(\rho\beta)_{nf} = (1-\phi)(\rho\beta)_{bf} + \phi(\rho\beta)_{np}. \tag{14}$$

The dynamic viscosity ratio of water alumina follows Corcione [35] model:

$$\frac{\mu_{nf}}{\mu_{bf}} = 1/\left(1 - 34.87\left(d_{np}/d_{bf}\right)^{-0.3}\phi^{1.03}\right). \tag{15}$$

The conductivity ratio of water alumina is calculated by Corcione [35] as follows:

$$\frac{k_{nf}}{k_{bf}} = 1 + 4.4Re_B^{0.4}Pr^{0.66}\left(\frac{T_{nf}}{T_{fr}}\right)^{10}\left(\frac{k_{np}}{k_{bf}}\right)^{0.03}\phi^{0.66}. \tag{16}$$

with parameter Re_B that has a function

$$Re_B = \frac{\rho_{bf}u_B d_{np}}{\mu_{bf}}, \tag{17}$$

$$u_B = \frac{2k_b T_{nf}}{\pi\mu_{bf}d_{np}^2}, \tag{18}$$

where constant k_b is given by Boltzmann. Constant $l_{bf} = 0.17$ nm is the mean path of the base fluid. d_{bf} is the molecular size of the host fluid given as Corcione [35].

$$d_{bf} = \frac{6M}{N\pi\rho_{bf}}, \tag{19}$$

where M is the molecular mass of the water, N is the Avogadro number, and ρ_{bf} is the density of the base liquid at our environment temperature. Value of d_{bf} is evaluated as

$$d_{bf} = \sqrt[3]{\frac{6 \times 0.01801528}{6.022 \times 10^{23} \times \pi \times 998.26}}. \tag{20}$$

Now, we introduce the following nondimensional variables:

$$X = \frac{x}{H}, Y = \frac{y}{H}, U = \frac{uH}{\nu_{bf}}, V = \frac{\nu H}{\nu_{bf}}, P = \frac{pH^2}{\rho_{nf}\nu_{bf}^2}, \Phi_{nf} = \frac{C_{nf}}{\phi},$$
$$D_B^* = \frac{D_B}{D_{B0}}, \delta = \frac{T_c}{T_h - T_c}, \Theta_{nf} = \frac{T_{nf} - T_c}{T_h - T_c}, D_T^* = \frac{D_T}{D_{T0}}, R = \frac{r}{H}. \tag{21}$$

This, then, yields the dimensionless continuity, momentum, energy, and nanoparticle equations:

$$\frac{\partial U}{\partial X} + \frac{\partial V}{\partial Y} = 0, \tag{22}$$

$$\left(\frac{\rho_{nf}}{\rho_{bf}}\right)\frac{U}{\varepsilon^2}\frac{\partial U}{\partial X} + \left(\frac{\rho_{nf}}{\rho_{bf}}\right)\frac{V}{\varepsilon^2}\frac{\partial U}{\partial Y} = -\left(\frac{\rho_{nf}}{\rho_{bf}}\right)\frac{\partial P}{\partial X} + \left(\frac{\mu_{nf}}{\mu_{bf}\varepsilon}\right)\left(\frac{\partial^2 U}{\partial X^2} + \frac{\partial^2 U}{\partial Y^2}\right) + \left(\frac{\rho_{nf}}{\rho_{bf}}\frac{\mu_{nf}}{\mu_{bf}}\right)\frac{U}{Da} - \left(\frac{\rho_{nf}}{\rho_{bf}}\frac{\mu_{nf}}{\mu_{bf}}\right)\frac{C_F}{\Pr}\frac{\sqrt{U^2+V^2}}{\sqrt{Da}}U, \tag{23}$$

$$\left(\frac{\rho_{nf}}{\rho_{bf}}\right)\frac{U}{\varepsilon^2}\frac{\partial V}{\partial X} + \left(\frac{\rho_{nf}}{\rho_{bf}}\right)\frac{V}{\varepsilon^2}\frac{\partial V}{\partial Y} = -\left(\frac{\rho_{nf}}{\rho_{bf}}\right)\frac{\partial P}{\partial Y} + \left(\frac{\mu_{nf}}{\varepsilon\mu_{bf}}\right)\left(\frac{\partial^2 V}{\partial X^2} + \frac{\partial^2 V}{\partial Y^2}\right) + \left(\frac{\rho_{nf}}{\rho_{l}}\frac{\mu_{nf}}{\mu_{l}}\right)\frac{V}{Da} - \left(\frac{\rho_{nf}}{\rho_{bf}}\frac{\mu_{nf}}{\mu_{bf}}\right)\frac{C_F}{\Pr}\frac{\sqrt{U^2+V^2}}{\sqrt{Da}}V + \left[\left(\frac{(\rho\beta)_{nf}}{(\rho\beta)_{bf}}\right)\frac{1}{\Pr}Ra\Theta\right], \tag{24}$$

$$\frac{U}{\varepsilon}\frac{\partial\Theta_{nf}}{\partial X} + \frac{V}{\varepsilon}\frac{\partial\Theta_{nf}}{\partial Y} = \frac{(\rho C_p)_{bf}}{(\rho C_p)_{nf}}\frac{k_{nf}}{k_{bf}}\frac{1}{\Pr}\left(\frac{\partial^2\Theta_{nf}}{\partial X^2} + \frac{\partial^2\Theta_{nf}}{\partial Y^2}\right) + \frac{(\rho C_p)_{bf}}{(\rho C_p)_{nf}}\frac{D_B^*}{\Pr Le}\cdot\left(\frac{\partial\Phi_{nf}}{\partial X}\frac{\partial\Theta_{nf}}{\partial X} + \frac{\partial\Phi_{nf}}{\partial Y}\frac{\partial\Theta_{nf}}{\partial Y}\right) + \frac{(\rho C_p)_{bf}}{(\rho C_p)_{nf}}\frac{D_T^*}{\Pr Le N_{BT}}\frac{1}{1+\delta\Theta_{nf}}\cdot\left[\left(\frac{\partial\Theta_{nf}}{\partial X}\right)^2 + \left(\frac{\partial\Theta_{nf}}{\partial Y}\right)^2\right], \tag{25}$$

$$U\frac{\partial\Phi_{nf}}{\partial X} + V\frac{\partial\Phi_{nf}}{\partial Y} = \frac{D_B^*\varepsilon}{Sc}\left(\frac{\partial^2\Phi_{nf}}{\partial X^2} + \frac{\partial^2\Phi_{nf}}{\partial Y^2}\right) + \frac{D_T^*}{ScN_{BT}}\frac{\varepsilon}{1+\delta\Theta_{nf}}\left(\frac{\partial^2\Theta_{nf}}{\partial X^2} + \frac{\partial^2\Theta_{nf}}{\partial Y^2}\right). \tag{26}$$

Parameters $D_{B0} = k_b T_c/3\pi\mu_{bf}d_p$ are the reference Brownian diffusion coefficient, $Sc = \nu_{bf}/D_{B0}$ is the Schmidt number, $D_{T0} = 0.26(k_{bf}/2k_{bf} + k_{np})(\mu_{bf}/\rho_{bf}\theta)\phi$ is the reference thermophoretic diffusion coefficient, $N_{BT} = \phi D_{B0}T_c/D_{T0}(T_h - T_c)$ is the diffusivity ratio parameter (Brownian diffusivity/thermophoretic diffusivity), $Le = k_{bf}/(\rho C_p)_{bf}\phi D_{B0}$ is the Lewis number, $Ra = g\rho_{bf}\beta_{bf}(T_h - T_c)H^3/\mu_{bf}\alpha_{bf}$ is the Rayleigh number, $Da = K/H^2$ is the Darcy number, and Prandtl number, Pr, is equal to ν_{bf}/α_{bf}, Forchheimer coefficient, C_F, is equal to $1.75/\sqrt{150}$, $K = \varepsilon^2 D_p^2/150[1-\varepsilon]^2$ is the permeability of the porous medium, D_p is spherical bead diameter [33], and $k_m = \varepsilon + (1-\varepsilon)k_{np}/k_{bf}$ is the matrix porous conductivity. The dimensionless boundary conditions are as follows:

$$U = V = 0, \frac{\partial\Phi_{nf}}{\partial n} = -\frac{D_T^*}{D_B^*}\cdot\frac{1}{N_{BT}}\cdot\frac{1}{1+\delta\Theta_{nf}}\frac{\partial\Theta_{nf}}{\partial n}, \Theta_{nf} = 1 \text{ on cylinder}, \tag{27}$$

$$U = V = 0, \frac{\partial\Phi_{nf}}{\partial n} = -\frac{D_T^*}{D_B^*}\cdot\frac{1}{N_{BT}}\cdot\frac{1}{1+\delta\Theta_{nf}}\frac{\partial\Theta_{nf}}{\partial n}, \Theta_{nf} = 0 \text{ on the walls}. \tag{28}$$

The dimensionless streamfunction is obtained using the relation $\partial\Psi/\partial Y = U$ and $\partial\Psi/\partial X = -V$. The local Nusselt number Nu evaluated at the sinusoidal surface is

$$Nu(\zeta) = -\frac{k_{nf}}{k_{bf}}\frac{\partial\Theta bf}{\partial\zeta}, \tag{29}$$

where ζ is the rotation coordinate. The averaged Nusselt number $\bar{N}u$ on the hot sinusoidal cylinder is computed by

$$\bar{N}u = \frac{1}{P_{\sin}}\int_0^{360} Nu(\zeta)d\zeta, \tag{30}$$

where $P_{\sin}$ is a perimeter of the sinusoidal cylinder. This perimeter is in the function of the amplitude and number of undulation, and here, the radius is kept at $R = 0.2$.

3. Computational Methodology

The Galerkin FEM method is used to solve numerically the mathematical equations in the form of PDEs to determine the fluid flows and thermal distribution inside the annulus. First, a strong formulation of the governing equation is established by discarding the pressure element using a penalty parameter λ and the continuity as the following

$$P = -\lambda\left(\frac{\partial U}{\partial X} + \frac{\partial V}{\partial Y}\right). \tag{31}$$

Strong formulation of the X momentum is stated as

$$\begin{aligned}
&\left(\frac{\rho_{nf}}{\rho_{bf}}\right)\frac{U}{\varepsilon^2}\frac{\partial U}{\partial X} + \left(\frac{\rho_{nf}}{\rho_{bf}}\right)\frac{V}{\varepsilon^2}\frac{\partial U}{\partial Y} \\
&\quad = -\left(\frac{\rho_{nf}}{\rho_{bf}}\right)\frac{\partial \lambda}{\partial X}\left(\frac{\partial U}{\partial X} + \frac{\partial V}{\partial Y}\right) + \left(\frac{\mu_{nf}}{\mu_{bf}\varepsilon}\right)\left(\frac{\partial^2 U}{\partial X^2} + \frac{\partial^2 U}{\partial Y^2}\right) \\
&\qquad + \left(\frac{\rho_{nf}}{\rho_{bf}}\frac{\mu_{nf}}{\mu_{bf}}\right)\frac{U}{Da} - \left(\frac{\rho_{nf}}{\rho_{bf}}\frac{\mu_{nf}}{\mu_{bf}}\right)\frac{C_F}{\Pr}\frac{\sqrt{U^2+V^2}}{\sqrt{Da}}U.
\end{aligned} \tag{32}$$

Strong formulation of the Y momentum is stated as

$$\begin{aligned}
&\left(\frac{\rho_{nf}}{\rho_{bf}}\right)\frac{U}{\varepsilon^2}\frac{\partial V}{\partial X} + \left(\frac{\rho_{nf}}{\rho_{bf}}\right)\frac{V}{\varepsilon^2}\frac{\partial V}{\partial Y} \\
&\quad = -\left(\frac{\rho_{nf}}{\rho_{bf}}\right)\frac{\partial \lambda}{\partial X}\left(\frac{\partial U}{\partial X} + \frac{\partial V}{\partial Y}\right) + \left(\frac{\mu_{nf}}{\varepsilon\mu_{bf}}\right)\left(\frac{\partial^2 V}{\partial X^2} + \frac{\partial^2 V}{\partial Y^2}\right) \\
&\qquad + \left(\frac{\rho_{nf}}{\rho_{bf}}\frac{\mu_{nf}}{\mu_{bf}}\right)\frac{V}{Da} - \left(\frac{\rho_{nf}}{\rho_{bf}}\frac{\mu_{nf}}{\mu_{bf}}\right)\frac{C_F}{\Pr}\frac{\sqrt{U^2+V^2}}{\sqrt{Da}}V \\
&\qquad + \left[\left(\frac{(\rho\beta)_{nf}}{(\rho\beta)_{bf}}\right)\frac{1}{\Pr}Ra\Theta\right].
\end{aligned} \tag{33}$$

If the multielement technique is used, the strong formulation must take the second derivative, which is a drawback.

Second, by multiplying the equations by a test function, weak formulations of the momentum equations are obtained. The adjusted momentum equations are then integrated over the domain. The weak form provides advantages in terms of computation flexibility. Third, the unknown function is estimated. Finally, expand the U, V, Θ_{nf}, and Φ_{nf} using basis function Φ as

$$\begin{aligned}
U \approx \sum_{k=1}^{N} U_k\Phi_k(X,Y),\ V \approx \sum_{k=1}^{N} V_k\Phi_k(X,Y),\ \Theta_{nf} \approx \sum_{k=1}^{N}\left(\Theta_{nf}\right)_k\Phi_k(X,Y), \\
\Phi_{nf} \approx \sum_{k=1}^{N}\left(\Phi_{nf}\right)_k\Phi_k(X,Y).
\end{aligned} \tag{34}$$

The nonlinear residual equations for the X momentum equation were generated from the Galerkin-weighted residual FEM at nodes of internal domain Ω that is

$$\begin{aligned}
R_i^{(1)} = &\left(\frac{\rho_{nf}}{\varepsilon^2\rho_{bf}}\right)\sum_{k=1}^{N} U_k\int_\Omega\left[\left(\sum_{k=1}^{N} U_k\Phi_k\right)\frac{\partial\Phi_k}{\partial X}\right. \\
&\left.+\left(\frac{\rho_{nf}}{\varepsilon^2\rho_{bf}}\right)\left(\sum_{k=1}^{N} V_k\Phi_k\right)\frac{\partial\Phi_k}{\partial Y}\right]\Phi_i dXdY + \left(\frac{\lambda\rho_{nf}}{\rho_{bf}}\right) \\
&\cdot\left[\sum_{k=1}^{N} U_k\int_\Omega\frac{\partial\Phi_i}{\partial X}\frac{\partial\Phi_k}{\partial X}\mathrm{d}X\mathrm{d}Y + \sum_{k=1}^{N} V_k\int_\Omega\frac{\partial\Phi_i}{\partial X}\frac{\partial\Phi_k}{\partial X}\mathrm{d}X\mathrm{d}Y\right] \\
&+\left(\frac{\mu_{nf}}{\varepsilon\mu_{bf}}\right)\sum_{k=1}^{N} U_k\int_\Omega\left[\frac{\partial\Phi_i}{\partial X}\frac{\partial\Phi_k}{\partial X} + \frac{\partial\Phi_i}{\partial Y}\frac{\partial\Phi_k}{\partial Y}\right]dXdY \\
&+\left(\frac{\rho_{nf}}{\rho_{bf}}\frac{\mu_{nf}}{\mu_{bf}}\right)\frac{1}{Da}\int_\Omega\left(\sum_{k=1}^{N} U_k\Phi_k\right)\Phi_i dXdY \\
&+\left(\frac{\rho_{nf}}{\rho_{bf}}\frac{\mu_{nf}}{\mu_{bf}}\right)\frac{C_F}{\sqrt{Da}\Pr}\left\{\left[\int_\Omega\left(\sum_{k=1}^{N} U_k\Phi_k\right)\Phi_i dXdY\right]^2\right. \\
&\left.+\left[\int_\Omega\left(\sum_{k=1}^{N} V_k\Phi_k\right)\Phi_i dXdY\right]^2\right\}^{0.5}\int_\Omega\left(\sum_{k=1}^{N} U_k\Phi_k\right)\Phi_i dXdY.
\end{aligned} \tag{35}$$

The nonlinear residual equations for the Y momentum equation is

$$\begin{aligned}
R_i^{(2)} = &\left(\frac{\rho_{nf}}{\varepsilon^2\rho_{bf}}\right)\sum_{k=1}^{N} V_k\int_\Omega\left[\left(\sum_{k=1}^{N} U_k\Phi_k\right)\frac{\partial\Phi_k}{\partial X}\right. \\
&\left.+\left(\frac{\rho_{nf}}{\varepsilon^2\rho_{bf}}\right)\left(\sum_{k=1}^{N} V_k\Phi_k\right)\frac{\partial\Phi_k}{\partial Y}\right]\Phi_i dXdY + \left(\frac{\lambda\rho_{nf}}{\rho_{bf}}\right) \\
&\cdot\left[\sum_{k=1}^{N} U_k\int_\Omega\frac{\partial\Phi_i}{\partial Y}\frac{\partial\Phi_k}{\partial X}\mathrm{d}X\mathrm{d}Y + \sum_{k=1}^{N} V_k\int_\Omega\frac{\partial\Phi_i}{\partial Y}\frac{\partial\Phi_k}{\partial Y}\mathrm{d}X\mathrm{d}Y\right] \\
&+\left(\frac{\mu_{nf}}{\varepsilon\mu_{bf}}\right)\sum_{k=1}^{N} V_k\int_\Omega\left[\frac{\partial\Phi_i}{\partial X}\frac{\partial\Phi_k}{\partial X} + \frac{\partial\Phi_i}{\partial Y}\frac{\partial\Phi_k}{\partial Y}\right]\mathrm{d}X\mathrm{d}Y \\
&+\left(\frac{\rho_{nf}}{\rho_{bf}}\frac{\mu_{nf}}{\mu_{bf}}\right)\frac{1}{Da}\int_\Omega\left(\sum_{k=1}^{N} V_k\Phi_k\right)\Phi_i dXdY \\
&+\left(\frac{\rho_{nf}}{\rho_{bf}}\frac{\mu_{nf}}{\mu_{bf}}\right)\frac{C_F}{\sqrt{Da}\Pr}\left\{\left[\int_\Omega\left(\sum_{k=1}^{N} U_k\Phi_k\right)\Phi_i dXdY\right]^2\right. \\
&\left.+\left[\int_\Omega\left(\sum_{k=1}^{N} V_k\Phi_k\right)\Phi_i dXdY\right]^2\right\}^{0.5}\int_\Omega\left(\sum_{k=1}^{N} V_k\Phi_k\right)\Phi_i dXdY \\
&+\left(\frac{(\rho\beta)_{nf}}{(\rho\beta)_{bf}}\right)\frac{Ra}{\Pr}\int_\Omega\left(\sum_{k=1}^{N}\left(\Theta_{nf}\right)_k\Phi_k\right)\Phi_i dXdY.
\end{aligned} \tag{36}$$

Table 2: Grid sensitivity check at $Ra = 10^5$, $\phi = 0.03$, $A = 0.2$, and $N = 5$.

Mesh size	Domain elements	Ψ_{min}	$\bar{Nu}$	CPU time (s)
M1	6329	-3.3058	6.7280	37
M2	9063	-3.2863	6.7210	60
M3	14127	-3.2716	6.7026	169
M4	31000	-3.2673	6.7249	214
M5	38498	-3.2673	6.7229	351

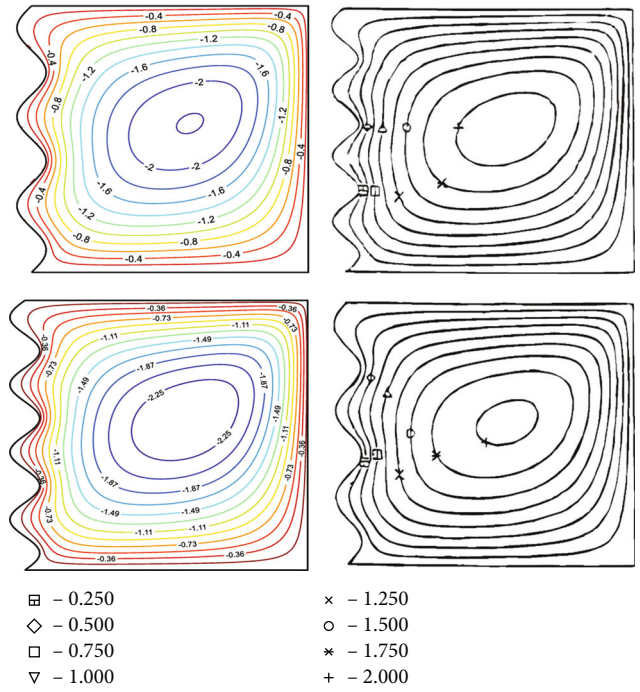

Figure 2: Validation of current streamlines with published [8] results for the sinusoidal undulated surface at $Da = 10^{-5}$, $\phi = 0.0$, $Ra = 5 \times 10^6$, $A = 0.05$, and $N = 4, 3$.

For both the test and basic functions, the Galerkin FEM employs the same function.

The residual integrations of the momentum and heat transfer, nanoparticle equations in X and Y directions are employed by using Gauss's method. A Newton-Raphson method is employed to solve the system nonlinear algebraic equations expressed in a matrix. The iteration of the current work is assumed to be a convergence solution when the corresponding error of each variable is equals or less than 10^{-6}. In heterogeneous distribution, triangular mesh element is selected to mesh all domains.

To get the optimal grid size, the mesh independency test is performed for $Ra = 10^5$, $\phi = 0.03$, $A = 0.2$, and $N = 5$ as tabulated in Table 2. The mesh sizes, i.e., M1, M2, M3, M4, and M5 are labelled for identification. The numbers inside the table are observed to be consistent by increasing the number of elements. Considering both time computation and the error, the M4 grid size was chosen for all the computations done in this paper. As a comparison, streamline results are validated with that reported by Kumar [8] for the sinusoidal undulated surface at $Da = 10^{-5}$, $\phi = 0.0$, $Ra = 5 \times 10^6$, $A = 0.05$, and $N = 4, 3$ as presented in Figure 2.

4. Results and Discussion

The analysis in this simulation is performed in the following domain of the related dimensionless quantities: the average alumina volume fraction, $0.0 \le \phi \le 0.04$; the amplitude of corrugated surface, $0 \le A \le 0.3$; the number of corrugated surface, $3 \le N \le 6$; and the Rayleigh number, $10^3 \le Ra \le 10^6$. The base radius is 0.2, the porosity is 0.7, the Darcy number is 0.02, the Prandtl number is 4.62, the Lewis number is 3.5E5, the normalized temperature is 155, the Schmidt number is 3.5E4, and the ratio of Brownian to thermophoretic diffusivity is 1.1. The alumina concentrations are varied in $0 \le \phi \le 0.04$ to avoid clogging in the system.

Figures 3 and 4 present the effects of various values of Rayleigh numbers and corrugated surface on streamlines and isotherms for $N = 4$ and $\phi = 0.03$. The heat transfer is majority by the conduction at the small Rayleigh number.

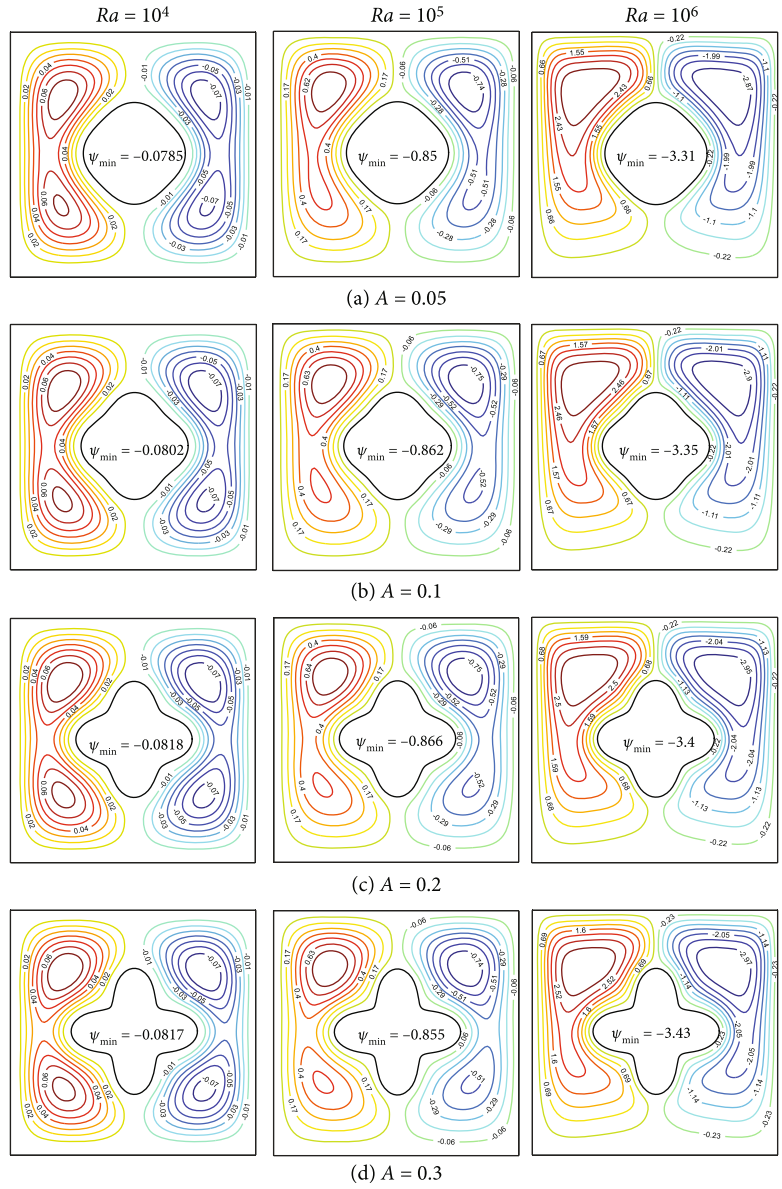

FIGURE 3: Streamlines for the combination of Rayleigh numbers and varying the amplitude corrugation, A at $N = 4$ and $\phi = 0.03$.

Hence, as seen in Figure 4 ($A = 0.05$), the thermal structures lay over each other circularly with minimum distortions. This figure exhibits almost a conduction mode of temperature from the hot sinusoidal cylinder to the cold enclosure. The plot of the streamlines exhibits a pair of rotating cells, which follows the pattern and location of the isotherm magnitude. By increasing the Rayleigh number, the convective flow becomes stronger where the hot fluid from the sinusoidal surface moves upward and keeps reaching the top wall and then moves along the left cold and right surfaces. At the upper part, the fluid losses its heat to the cold wall and then circulates down next to the left and right wall. Due to the fluid movement transporting mass transfer, the isotherms have deflected along with the fluid flow, and the isotherm magnitude has shifted toward the top. Increasing the heating intensity leads to a higher flow circulation. The movement of the fluid follows how the heating changes and meets up with how its enthalpy changes. The streamlines show a pair circulation surrounding the undulated circle with the vortices moving upward. When the flows rotated as cells in the clockwise direction, the maximum value of the flow circulation is attributed by $\Psi_{\min}$. The streamline magnitude is stagnant by adjusting the undulated amplitude. This indicates that the undulated wall seems unsensitive to the velocities. At $Ra = 10^5$ and $Ra = 10^6$, single vortices developed on the left and right sides of the annulus. Later, at larger amplitudes, double vortices formed at $Ra = 10^5$ occupy the annulus's left and right halves. The vortices have the form of a vertical ellipse. This is due to the inner heat circulation in the free space between the cylinder and the left and right walls being modified by the amplitude especially at moderate heating intensity. The local decreasing of temperature gradient brings to the upwelling plume.

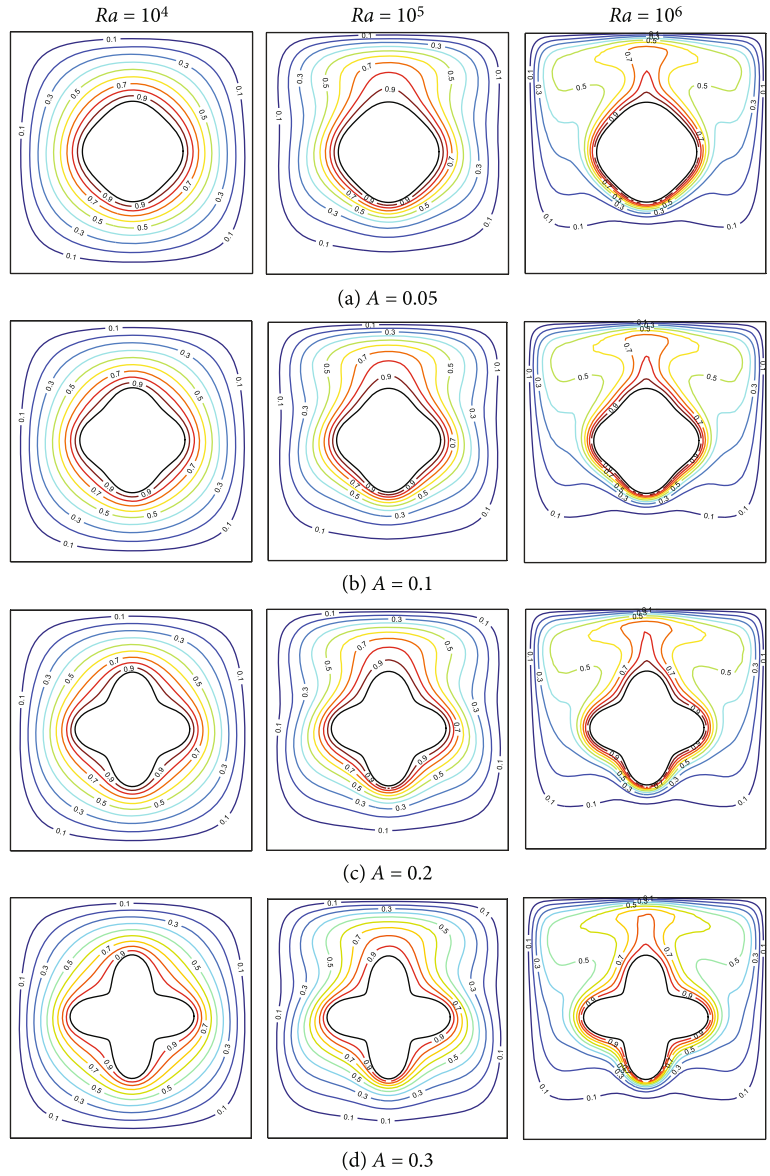

FIGURE 4: Isotherms for the combination of Rayleigh numbers and varying the amplitude corrugation, A at $N = 4$ and $\phi = 0.03$.

Figures 5 and 6 show the influence of several values of Rayleigh numbers and corrugated surface on streamlines and isotherms for $A = 0.2$ and $\phi = 0.03$. Single vortices appeared at the left and right part of the annulus at $N = 3$. Later at higher undulation number, double vortices generated by gravitational acceleration occupy the left and right part of the annulus. The shape of the vortices is a vertical ellipse. At $Ra = 10^6$, both flow circulations shift to the top wall and change to an almost like elliptical shape which denser lines with high intensity at the upper part of the annulus. The value of the flow circulation decreases by the rise of undulated number, and the same circulations tend to grow vertically because of modifying the hot zone. The hot nanofluids were transferred via conduction at $N = 3$ and the small Rayleigh number. At $N = 4$, the isotherms very near to cylinder surface tend to take a circular-parallel shape which is at a small Rayleigh number. Taking Ra higher, the thermal distributions shift to the top wall with raising the density at the upper part. At $Ra = 10^6$, the generating force for starting the heat transfer is more strong and apparent, the isotherm pattern transfers to the curved shape. Very dense isotherm distributes above the wavy cylinder. This indicates the large temperature gradient near the top centerline. The mushroom shapes were obtained. The isotherm expands due to the great circulation that hits the top wall. This circulation was boosted by rising maximum heat transport because of increasing the hot surface from adding an undulated number. The streamlines and isotherms are symmetric along the geometric centerline.

Figure 7 shows the influence of combination values of Rayleigh numbers and varying the corrugation amplitude, A, and number, N, at $\phi = 0.03$. It observes that the alumina

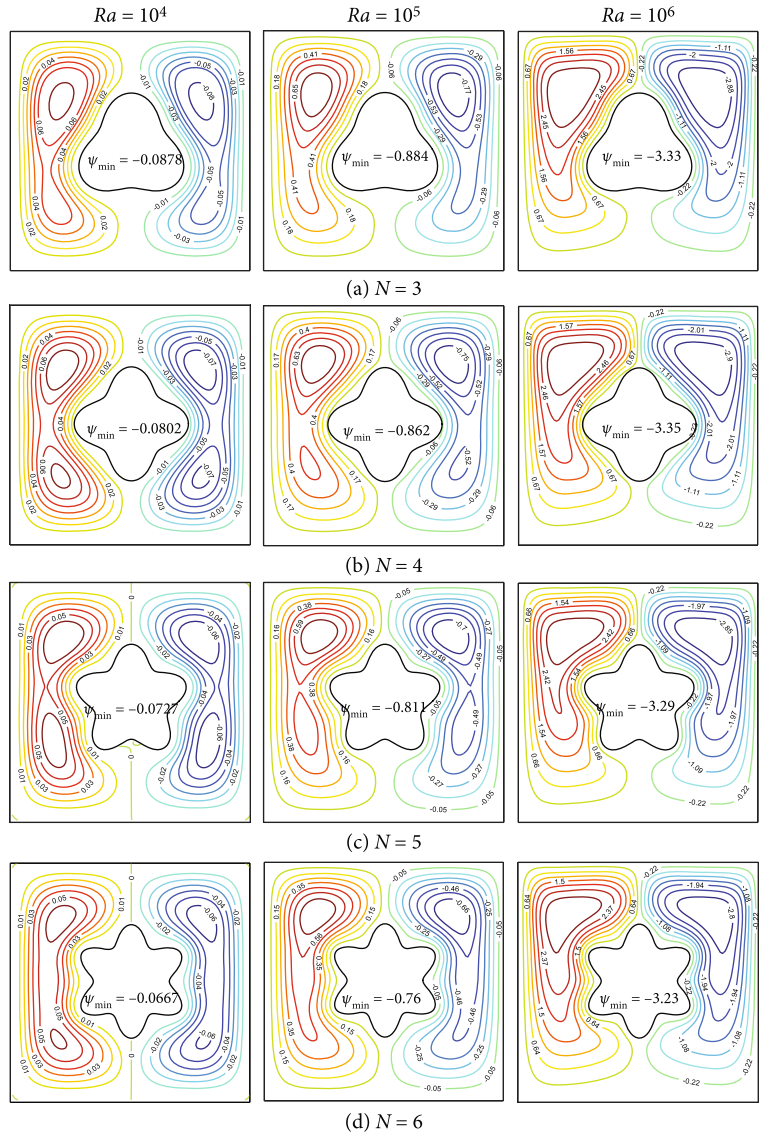

Figure 5: Streamlines for several Rayleigh numbers and varying the undulation number, N at $A = 0.2$ and $\phi = 0.03$.

concentration near the isothermal surfaces is higher than the concentration in the middle. The number of lines with high concentration below the corrugated cylinder increases when the amplitude or number of the corrugation takes higher. This figure shows that the aluminas are distributed uniformly at small Rayleigh number for various combinations of the amplitude and number undulations. Low heating intensity distributes the alumina in a large part of the annulus and homogenizes the solution. Here, the homogeneous nanofluid model could be valid since the insignificant effect of thermophoretic. When the cylinder heat is intensified, the thermal agitation and the circulation are great power at the lower part of the annulus. Furthermore, at a higher Rayleigh number, there is a small concentration gradient below the corrugated cylinder. Thus, the thermophoretic action that causes the dispersing of alumina has a low impact, and the agitation is not great in this area. It also observed denser nanoparticle distribution at this region. When the amplitude is higher at $N = 5$, the agitation of the alumina is improved. The enhancement of agitation causes a greater uniform alumina dispersion in the whole annulus. The improved agitation is a consequence of the increase in the length of heated surface. In the domains of convective cells, there are extensive uniform regions, whereas the nonuniform regions become more limited as they approach the corrugated surface.

Figure 8 shows a relationship between the mean Nusselt number, $\bar{Nu}$, and the Rayleigh number, Ra, at various ϕ when $N = 3$ and $A = 0.2$. Heat transfer rate increases with increasing the alumina volume fraction. The increasing more pronounced at a high and small Rayleigh number. This fact due to alumina thermal conductivity has a significant effect on increasing the thermal gradient at moderate buoyancy force, but the viscosity and agitation suppress the fluid movement. At the high Rayleigh number, intensity of the upper convective cells enhances considerably, and the sizes of regions with dense concentration decrease.

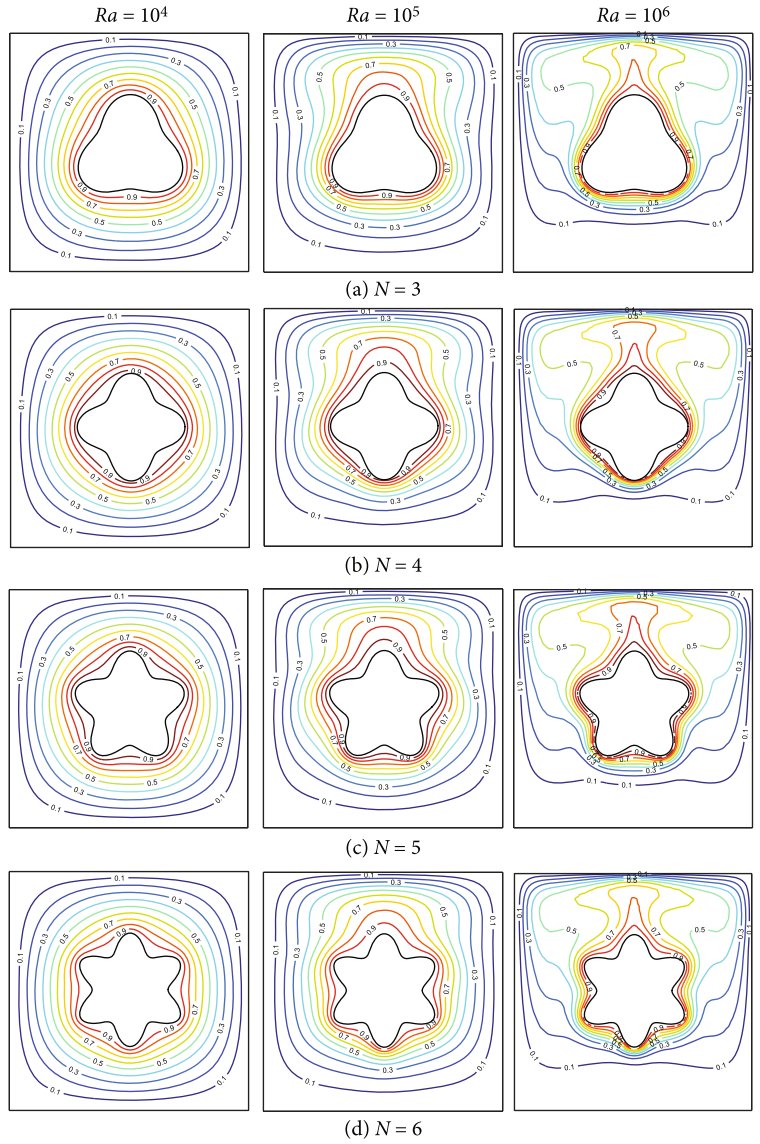

FIGURE 6: Isotherms for different Rayleigh numbers and varying the undulation number, N at $A = 0.2$ and $\phi = 0.03$.

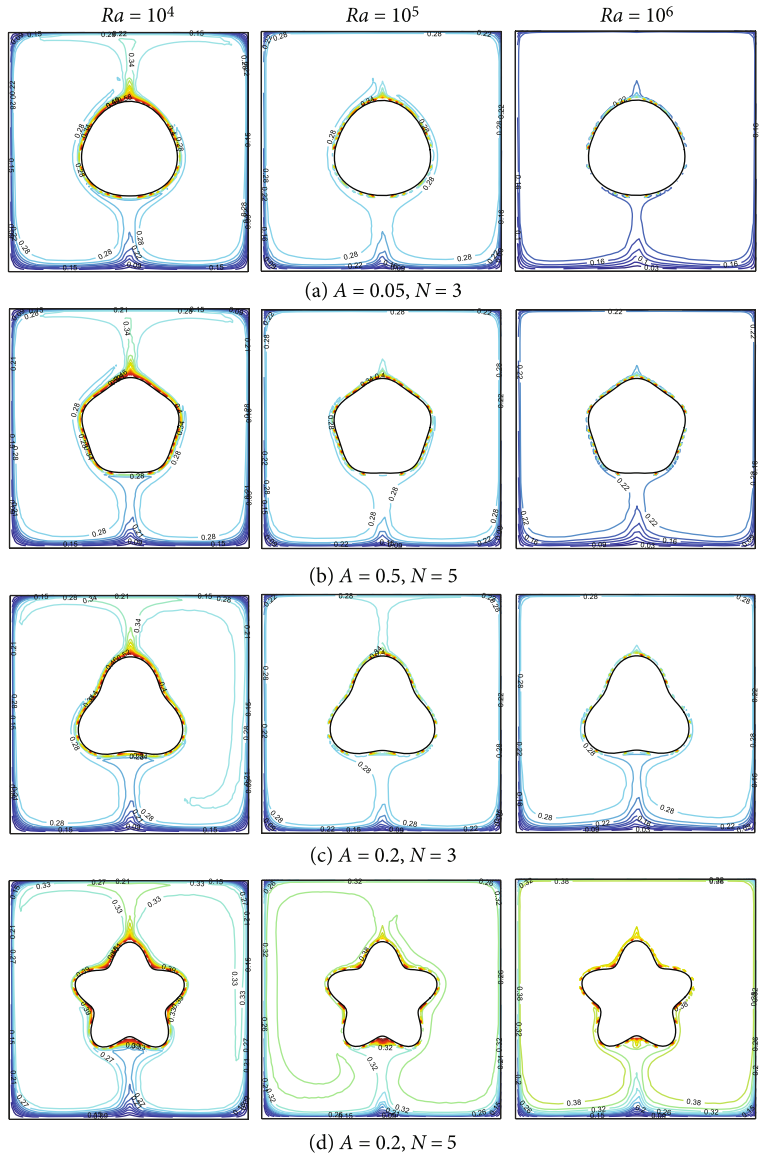

(a) $A = 0.05$, $N = 3$

(b) $A = 0.5$, $N = 5$

(c) $A = 0.2$, $N = 3$

(d) $A = 0.2$, $N = 5$

Figure 7: Alumina distribution for combination values of Rayleigh numbers and corrugation amplitude, A, and number, N, at $\phi = 0.03$.

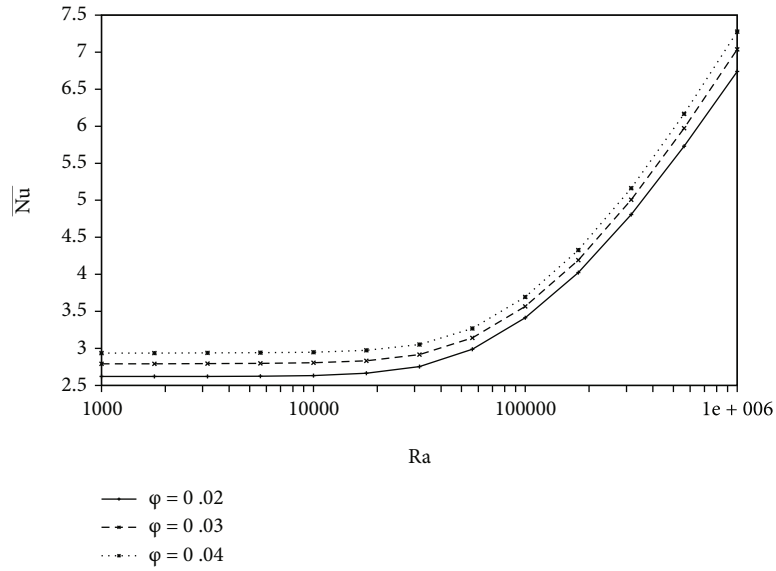

Figure 8: Plots of the average Nusselt number against Rayleigh number for the values of ϕ labelled on the figure at $N = 3$ and $A = 0.2$.

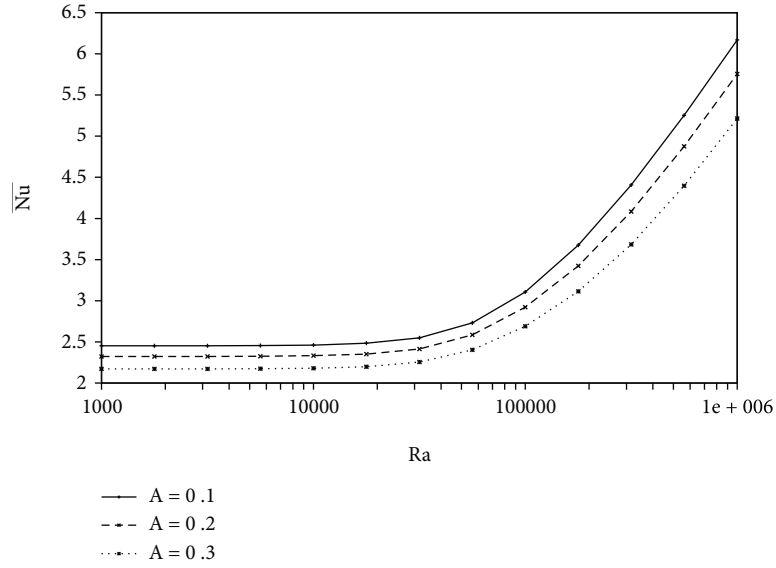

Figure 9: Influence of Rayleigh number and the corrugation amplitude on the average Nusselt number at $N = 4$ and $\phi = 0.03$.

The viscosity action and agitation are to suppress the flow circulation. The cumulative impact is to increase the Nusselt number considerably.

Figure 9 summarizes the variations of the average Nusselt number versus the Rayleigh number for different undulation amplitude at $N = 4$ and $\phi = 0.03$. The heat transfer rate decreases by increasing the amplitude, and it is being significant at a high heating intensity. The temperature gradient of the active wall reduces as the corrugation amplitude increases. The thermal performance follows the flow inhibition near the corrugated region where the flat wall is the best option. Isotherm changed (see Figure 4) because the Brownian motion parameter went up, which led to an unnecessary drop in the average Nusselt number.

Figure 10 summarizes the variations of average Nusselt number versus the Rayleigh number from 10^3 to 10^6 for various undulation number at $A = 0.2$ and $\phi = 0.03$. The Nusselt number is reduced by applying the undulated cylinder at any heating condition. Increasing undulated number decreases the heat transfer rate constantly from low to moderate Rayleigh number. The heat transfer rate decreases by increasing the waviness, and it is being significant at a high heating intensity. Increasing the waviness frequency to the thermal performance is equivalent with increasing the amplitude as mentioned in the previous case. At higher buoyancy force, increasing the undulation number decreases the thermal gradient, but the free space becomes larger. It is also supported by the fact that the

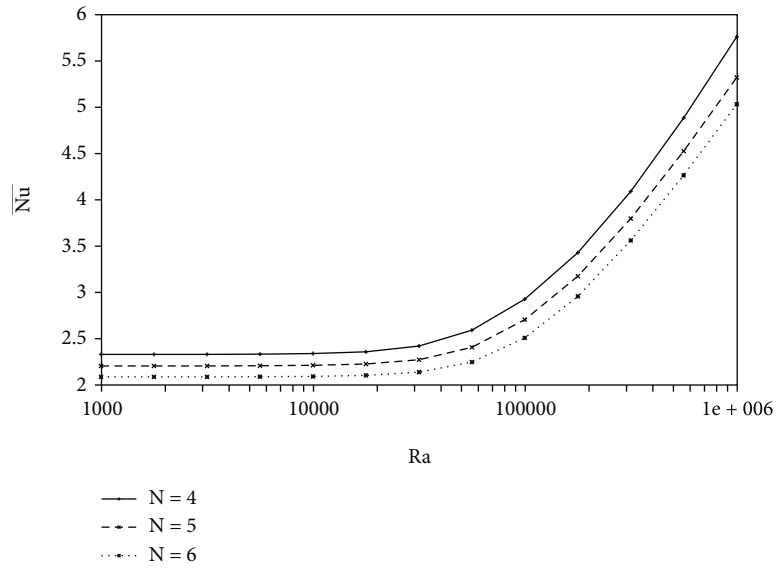

Figure 10: Impact of Rayleigh number and the undulation number on the average Nusselt number at $A = 0.2$ and $\phi = 0.03$.

Table 3: Differences in the average Nusselt number and Rayleigh number for different values of the controlling parameters, ϕ, A, and N.

Ra	ϕ	$N = 3$		$N = 5$	
		$A = 0.005$	$A = 0.2$	$A = 0.005$	$A = 0.2$
10^3	0	2.5109	2.4121	2.5155	2.1995
	0.01	2.8325	2.7211	2.8377	2.4812
	0.02	3.0191	2.9003	3.0246	2.6446
	0.03	3.1750	3.0501	3.1808	2.7812
	0.04	3.3138	3.1835	3.3199	2.9029
10^4	0	2.5262	2.4269	2.5304	2.2105
	0.01	2.8457	2.7338	2.8506	2.4907
	0.02	3.0312	2.9120	3.0364	2.6533
	0.03	3.1862	3.0609	3.1918	2.7892
	0.04	3.3244	3.1936	3.3302	2.9104
10^5	0	3.4154	3.2253	3.4215	2.8980
	0.01	3.7049	3.5090	3.7108	3.1528
	0.02	3.8652	3.6672	3.8710	3.2949
	0.03	3.9962	3.7967	4.0019	3.4115
	0.04	4.1109	3.9103	4.1165	3.5139
10^6	0	6.7172	6.2814	6.7380	5.7093
	0.01	7.3218	6.8445	7.3447	6.2170
	0.02	7.6542	7.1536	7.6784	6.4956
	0.03	7.9232	7.4034	7.9487	6.7210
	0.04	8.1567	7.6200	8.1833	6.9165

nanoparticle isoconcentrations are distributed heterogeneously at a relative large buoyancy force.

Differences in the average Nusselt number and Rayleigh number are shown in Table 3 for different values of the controlling parameters, ϕ, A, and N. The average Nusselt number increases significantly as the solid volume fraction increases. As can be seen from the table, the amplitude goes up, and the average rate of heat transfer goes down. The maximum rate of heat transfer takes place at $Ra = 10^6$, $A = 0.005$, and $N = 5$. The heat transfer rate varies almost linearly with the solid volume percentage. Increasing the solid concentration from 0 to 0.01 results in a 13% improvement in heat transfer rate at $Ra = 10^3$ and $Ra = 10^4$. Increasing the solid concentration from 0 to 0.01 results in a 9% improvement in heat transfer rate at $Ra = 10^5$ and $Ra = 10^6$.

5. Conclusions

Free convection of nanofluids induced by different temperature levels between cold walls and a hot sinusoidal cylinder was studied numerically. The continuity, Brinkman-Forchheimer flow, and energy equation inside the annulus are formulated in the dimensionless form. Two-phase Buongiorno nanofluid model was applied for the nanofluid layer. These equations were solved by the Galerkin FEM. Computed results of the flow fields and temperature distributions, as well as the heat transfer rate, are depicted graphically. The undulation frequencies, alumina volume fraction, and Rayleigh number affected the shape of streamlines, isotherms, isoconcentrations, and Nusselt number plots. Some important points from the study are given below:

(1) The intensity of the flow movement reduces as the undulated number increases but is stagnant with varying the undulated amplitude

(2) Shape, position, and number of the vortices depend on the waviness frequency and Rayleigh number. The nanoparticle isoconcentrations are not symmetric along the geometric centerline while the streamlines and isotherms are symmetric along the centerline

(3) Homogeneous nanofluid model could be valid for low heating intensity with higher amplitude and number of corrugation conditions

(4) The higher the alumina concentration, the higher the heat transfer rate. The heat transfer rate can be boosted by up to 13% by suspending 1% alumina particles. The heat transfer enhancement decreases with increasing the amplitude and/or increasing the waviness number

Abbreviations

Nomenclature

A: Undulation amplitude (m)
C_p: Heat capacity (J kg^{-1} K^{-1})
C_F: Forchheimer constant
Da: Darcy number
D_B: Brownian diffusion coefficient (kg m^{-1} s^{-1})
d_p: Diameter of the nanoparticle (nm)
D_T: Thermophoretic diffusivity coefficient (kg m^{-1} s^{-1}))
g: Gravitational force (m s^{-2})
k: Thermal conductivity (W m^{-1} K^{-1})
K: Permeability (m^2)
H: Length of enclosure (m)
N: Undulation number
p: Pressure (Pa)
P: Perimeter (m)
Pr: Prandtl number
r: Cylinder radius (m)
Ra: Rayleigh number or heating intensity
T: Temperature (K)
u, v: Velocity components in the x- and y-directions (m/s)
x, y, X, Y: Space coordinates (m) and dimensionless space coordinates.

Greek Symbols

α: Thermal diffusivity (m^2/s)
β: Thermal expansion coefficient (1/K)
ε: Porosity
Θ: Dimensionless temperature
ν: Kinematic viscosity (m^2/s)
ρ: Density (kg/m^3)
ϕ: Solid volume fraction
ψ: Stream function (m^2/s)
μ: Dynamic viscosity (kg m^{-1} s^{-1}).

Subscript

c: Cold
bf: Base fluid
h: Hot
nf: Nanofluid
np: Alumina nanoparticles
sin: Sinusoidal cylinder.

Data Availability

The data used to support the findings of this study are included in this paper and available without any restrictions.

Conflicts of Interest

The authors declare that there is no conflict of interests regarding the publication of this research article.

References

[1] P. H. Oosthuizen and D. Naylor, "Natural convective heat transfer from a cylinder in an enclosure partly filled with a porous medium," *International Journal of Numerical Methods for Heat & Fluid Flow*, vol. 6, pp. 51–63, 1996.

[2] A. Misirlioglu, "The effect of rotating cylinder on the heat transfer in a square cavity filled with porous medium," *International Journal of Engineering Science*, vol. 44, no. 18-19, pp. 1173–1187, 2006.

[3] H. Saleh and I. Hashim, "Natural convection from a cylinder in square porous enclosure filled with nanofluids," *Journal of Porous Media*, vol. 18, no. 6, pp. 559–567, 2015.

[4] A. Alhashash, "Natural convection of nanoliquid from a cylinder in square porous enclosure using Buongiorno's two-phase model," *Scientific Reports*, vol. 10, no. 1, pp. 1–12, 2020.

[5] T. Tayebi and A. J. Chamkha, "Analysis of the effects of local thermal non-equilibrium (LTNE) on thermo- natural convection in an elliptical annular space separated by a nanofluid-saturated porous sleeve," *International Communications in Heat and Mass Transfer*, vol. 129, article 105725, 2021.

[6] T. Tayebi, A. J. Chamkha, H. F. Oztop, and L. Bouzeroura, "Local thermal non-equilibrium (LTNE) effects on thermal-free convection in a nanofluid-saturated horizontal elliptical non-darcian porous annulus," *Mathematics and Computers in Simulation*, vol. 194, pp. 124–140, 2022.

[7] P. V. S. N. Murthy, B. V. Rathish Kumar, and P. Singh, "Natural convection heat transfer from a horizontal wavy surface in a porous enclosure," *Numerical Heat Transfer, Part A Applications*, vol. 31, no. 2, pp. 207–221, 1997.

[8] B. V. R. Kumar, "A study of free convection induced by a vertical wavy surface with heat flux in a porous enclosure," *Numerical Heat Transfer: Part A: Applications*, vol. 37, no. 5, pp. 493–510, 2000.

[9] B. V. R. Kumar, "Non-Darcy free convection induced by a vertical wavy surface in a thermally stratified porous medium," *International Journal of Heat and Mass Transfer*, vol. 47, no. 10-11, pp. 2353–2363, 2004.

[10] A. Misirlioglu, A. C. Baytas, and I. Pop, "Free convection in a wavy cavity filled with a porous medium," *International Journal of Heat and Mass Transfer*, vol. 48, no. 9, pp. 1840–1850, 2005.

[11] A. Misirlioglu, A. C. Baytas, and I. Pop, "Natural convection inside an inclined wavy enclosure filled with a porous medium," *Transport in Porous Media*, vol. 64, no. 2, pp. 229–246, 2006.

[12] K. Khanafer, B. Al-Azmi, A. Marafie, and I. Pop, "Non-Darcian effects on natural convection heat transfer in a wavy porous enclosure," *International Journal of Heat and Mass Transfer*, vol. 52, no. 7-8, pp. 1887–1896, 2009.

[13] K. S. Mushatet, "Investigation of natural convection inside an inclined porous square cavity with two wavy walls," *Global Journal of Research In Engineering*, vol. 10, no. 6, 2010.

[14] M. A. Mansour, M. M. A. El-Aziz, R. A. Mohamed, and S. E. Ahmed, "Numerical simulation of natural convection in wavy porous cavities under the influence of thermal radiation using a thermal non-equilibrium model," *Transport in porous media*, vol. 86, no. 2, pp. 585–600, 2011.

[15] P. Sompong and S. Witayangkurn, "Numerical study of natural convection in a heated enclosure with two wavy vertical walls using finite element method," *Journal of Applied Mathematics*, vol. 2014, Article ID 853231, 9 pages, 2014.

[16] M. A. Sheremet, C. Revnic, and I. Pop, "Free convection in a porous wavy cavity filled with a nanofluid using Buongiorno's mathematical model with thermal dispersion effect," *Applied Mathematics and Computation*, vol. 299, pp. 1–15, 2017.

[17] H. T. Cheong, S. Sivasankaran, and M. Bhuvaneswari, "Natural convection in a wavy porous cavity with sinusoidal heating and internal heat generation," *International Journal of Numerical Methods for Heat & Fluid Flow*, vol. 27, no. 2, pp. 287–309, 2017.

[18] G. Hoghoughi, M. Izadi, H. F. Oztop, and N. Abu-Hamdeh, "Effect of geometrical parameters on natural convection in a porous undulant- wall enclosure saturated by a nanofluid using Buongiorno's model," *Journal of Molecular Liquids*, vol. 255, pp. 148–159, 2018.

[19] A. Alhashash and H. Saleh, "Natural convection induced by undulated surfaces in a porous enclosure filled with nanoliquid," *Advances in Mechanical Engineering*, vol. 11, no. 9, 2019.

[20] A. Alhashash, "Free convection from a corrugated heated cylinder with nanofluids in a porous enclosure," *Advances in Mechanical Engineering*, vol. 12, no. 8, 2020.

[21] A. I. Alsabery, T. Tayebi, R. Roslan, A. J. Chamkha, and I. Hashim, "Entropy generation and mixed convection flow inside a wavy-walled enclosure containing a rotating solid cylinder and a heat source," *Entropy*, vol. 22, no. 6, p. 606, 2020.

[22] A. I. Alsabery, T. Tayebi, A. J. Chamkha, and I. Hashim, "Effects of non-homogeneous nanofluid model on natural convection in a square cavity in the presence of conducting solid block and corner heater," *Energies*, vol. 11, no. 10, p. 2507, 2018.

[23] A. I. Alsabery, T. Tayebi, A. J. Chamkha, and I. Hashim, "Effects of two-phase nanofluid model on natural convection in a square cavity in the presence of an adiabatic inner block and magnetic field," *International Journal of Numerical Methods for Heat & Fluid Flow*, vol. 28, no. 7, 2018.

[24] A. Ghasemian, S. Dinarvand, A. Adamian, and M. A. Sheremet, "Unsteady general three-dimensional stagnation point flow of a Maxwell/Buongiorno non-Newtonian nanofluid," *Journal of Nanofluids*, vol. 8, no. 7, pp. 1544–1559, 2019.

[25] F. Hoseininejad, S. Dinarvand, and M. E. Yazdi, "Manninen's mixture model for conjugate conduction and mixed convection heat transfer of a nanofluid in a rotational/stationary circular enclosure," *International Journal of Numerical Methods for Heat & Fluid Flow*, vol. 31, no. 5, pp. 1662–1694, 2021.

[26] S. A. Nabavizadeh, S. Talebi, M. Sefid, and M. Nourmohammadzadeh, "Natural convection in a square cavity containing a sinusoidal cylinder," *International journal of thermal sciences*, vol. 51, pp. 112–120, 2012.

[27] M. Sheikholeslami, M. G. Bandpy, I. Pop, and S. Soleimani, "Numerical study of natural convection between a circular enclosure and a sinusoidal cylinder using control volume based finite element method," *International journal of thermal sciences*, vol. 72, pp. 147–158, 2013.

[28] M. Hatami and H. Safari, "Effect of inside heated cylinder on the natural convection heat transfer of nanofluids in a wavy-wall enclosure," *International Journal of Heat and Mass Transfer*, vol. 103, pp. 1053–1057, 2016.

[29] I. Hashim, A. I. Alsabery, M. A. Sheremet, and A. J. Chamkha, "Numerical investigation of natural convection of Al_2O_3 -water nanofluid in a wavy cavity with conductive inner block using Buongiorno's two-phase model," *Advanced Powder Technology*, vol. 30, no. 2, pp. 399–414, 2019.

[30] B. Jabbaripour, M. N. Rostami, S. Dinarvand, and I. Pop, "Aqueous aluminium-copper hybrid nanofluid flow past a sinusoidal cylinder considering three-dimensional magnetic field and slip boundary condition," *Proceedings of the Institution of Mechanical Engineers, Part E: Journal of Process Mechanical Engineering*, p. 095440892110464, 2021.

[31] T. Tayebi and A. J. Chamkha, "Effects of various configurations of an inserted corrugated conductive cylinder on MHD natural convection in a hybrid nanofluid-filled square domain," *Journal of Thermal Analysis and Calorimetry*, vol. 143, no. 2, pp. 1399–1411, 2021.

[32] S. P. Jang and S. D. S. Choi, "Effects of various parameters on nanofluid thermal conductivity," *Journal of Heat Transfer*, vol. 129, no. 5, pp. 617–623, 2007.

[33] P. Nithiarasu, K. N. Seetharamu, and T. Sundararajan, "Natural convective heat transfer in a fluid saturated variable porosity medium," *International Journal of Heat and Mass Transfer*, vol. 40, no. 16, pp. 3955–3967, 1997.

[34] J. Buongiorno, "Convective transport in nanofluids," *Journal of Heat Transfer*, vol. 128, no. 3, pp. 240–250, 2006.

[35] M. Corcione, "Empirical correlating equations for predicting the effective thermal conductivity and dynamic viscosity of nanofluids," *Energy Conversion and Management*, vol. 52, no. 1, pp. 789–793, 2011.